Title

Integrated platform for multiscale molecular imaging and phenotyping of the human brain.

Journal

The Scientific monthly, 384(6701)

Authors

Park, Juhyuk
Wang, Ji
Guan, Webster
et al.

Publication Date

2024-06-14

DOI

10.1126/science.adh9979

Peer reviewed

HHS Public Access

Author manuscript

Science. Author manuscript; available in PMC 2025 February 16.

Published in final edited form as:

Science. 2024 June 14; 384(6701): eadh9979. doi:10.1126/science.adh9979.

Integrated platform for multiscale molecular imaging and phenotyping of the human brain

Juhyuk Park[1,2,3,4,†,‡], **Ji Wang**[1,3,†], **Webster Guan**[2,†], **Lars A. Gjesteby**[5], **Dylan Pollack**[5], **Lee Kamentsky**[1,3], **Nicholas B. Evans**[1,3], **Jeff Stirman**[6], **Xinyi Gu**[7], **Chuanxi Zhao**[3], **Slayton Marx**[3], **Minyoung E. Kim**[8], **Seo Woo Choi**[2], **Michael Snyder**[5], **David Chavez**[5], **Clover Su-Arcaro**[3], **Yuxuan Tian**[2], **Chang Sin Park**[9,10], **Qiangge Zhang**[11], **Dae Hee Yun**[8], **Mira Moukheiber**[3], **Guoping Feng**[8,11], **X. William Yang**[9,10], **C. Dirk Keene**[12], **Patrick R. Hof**[13], **Satrajit S. Ghosh**[8,11,14], **Matthew P. Frosch**[15], **Laura J. Brattain**[5], **Kwanghun Chung**[1,2,3,8,*]

[1]Institute for Medical Engineering and Science, Massachusetts Institute of Technology (MIT), Cambridge, MA 02139, USA.

[2]Department of Chemical Engineering, MIT, Cambridge, MA 02139, USA.

[3]Picower Institute for Learning and Memory, MIT, Cambridge, MA 02139, USA.

[4]Center for Nanomedicine, Institute for Basic Science, Seoul 03722, Republic of Korea.

[5]MIT Lincoln Laboratory, Lexington, MA 02421, USA.

[6]LifeCanvas Technologies, Cambridge, MA 02141, USA.

[7]Department of Electrical Engineering and Computer Science, MIT, Cambridge, MA 02139, USA.

[*]**Corresponding author.** khchung@mit.edu.

[†]These authors contributed equally to this work.

[‡]Present address: Research Institute of Advanced Materials (RIAM), Department of Materials Science and Engineering, Seoul National University, Seoul 08826, Republic of Korea.

Author contributions: J.P., J.W., W.G., and K.C. conceived of the idea and designed the experiments. J.P., J.W., W.G., and K.C. designed the platform and wrote the paper with input from other authors. J.P. developed the mELAST technology and performed processing, staining, and imaging of the tissues. J.W. developed MEGAtome and the tissue-embedding method and sliced the tissues. W.G. developed UNSLICE and performed interslab stitching of the images. N.B.E. and J.S. developed MegaSPIM. L.K. developed the computational pipeline for processing MegaSPIM images with help from M.M. L.K. developed the algorithm for co-registration of multiround images. L.A.G., D.P., M.S., D.C., and L.J.B. developed the deep learning–based axon tracing algorithm and performed axon tracing on datasets with help from W.G. X.G. performed quantitative analysis of cells. C.Z. segmented the slab images. S.S.G. developed the DANDI platform. S.M. and M.M. managed data storage. L.K. and S.S.G. were involved with standardizing the data. L.K., S.M., and S.S.G. curated, organized, and made the data available on DANDI. M.E.K. helped enhance image quality and performed synapse counting. W.G. stitched and postprocessed MegaSPIM images. J.W. designed tissue pumps and photobleachers and assembled them with help from C.Z. S.W.C. and J.P. developed the slab-scale SHIELD-clearing protocol. J.P. co-registered multiround images. J.P. screened and validated antibodies with help from D.H.Y. Y.T. prepared SeTau647-conjugated secondary antibodies. J.P. formulated the refractive index-matching media. C.S.-A. helped buffer preparation. C.S.P. and X.W.Y. provided MORF mouse brain samples. Q.Z. and G.F. provided marmoset brain samples. M.P.F. provided the human brain tissue specimens. M.P.F., C.D.K., and P.R.H. helped with data interpretation. K.C. supervised all aspects of the work.

Competing interests: K.C. is a co-inventor on patent applications owned by MIT covering the SHIELD and SWITCH technology (PCT/US2016/064538, “Methods for controlling chemical reaction kinetics and interaction time in large systems”), the MAP technology (US Provisional Patent Application 62/330,018, “Methods for reversible and tunable tissue magnification”), and the ELAST technology (US Patent Application 17/308,462, “Compositions and methods relating to reversibly compressible tissue-hydrogel hybrids”). K.C. and J.W. are co-inventors on patent applications owned by MIT covering the MEGAtome technology. MegaSPIM uses patented axial sweeping technology (US10989661B2, “Uniform and scalable light-sheets generated by extended focusing”). K.C. is a cofounder of LifeCanvas Technologies, a start-up that provides solutions for 3D tissue processing and analysis.

[8]Department of Brain and Cognitive Sciences, MIT, Cambridge, MA 02139, USA.

[9]Department of Psychiatry and Biobehavioral Sciences, David Geffen School of Medicine at UCLA, Los Angeles, CA 90095, USA.

[10]Center for Neurobehavioral Genetics, Jane and Terry Semel Institute for Neuroscience, University of California, Los Angeles, CA 90024, USA.

[11]McGovern Institute for Brain Research, MIT, Cambridge, MA 02139, USA.

[12]Department of Laboratory Medicine and Pathology, University of Washington School of Medicine, Seattle, WA 98115, USA.

[13]Nash Family Department of Neuroscience, Center for Discovery and Innovation, and Friedman Brain Institute, Icahn School of Medicine at Mount Sinai, New York, NY 10019, USA.

[14]Department of Otolaryngology, Harvard Medical School, Boston, MA 02114, USA.

[15]C. S. Kubik Laboratory for Neuropathology, Massachusetts General Hospital and Harvard Medical School, Boston, MA 02114, USA.

Abstract

Understanding cellular architectures and their connectivity is essential for interrogating system function and dysfunction. However, we lack technologies for mapping the multiscale details of individual cells and their connectivity in the human organ–scale system. We developed a platform that simultaneously extracts spatial, molecular, morphological, and connectivity information of individual cells from the same human brain. The platform includes three core elements: a vibrating microtome for ultraprecision slicing of large-scale tissues without losing cellular connectivity (MEGAtome), a polymer hydrogel–based tissue processing technology for multiplexed multiscale imaging of human organ–scale tissues (mELAST), and a computational pipeline for reconstructing three-dimensional connectivity across multiple brain slabs (UNSLICE). We applied this platform for analyzing human Alzheimer's disease pathology at multiple scales and demonstrating scalable neural connectivity mapping in the human brain.

Abstract

INTRODUCTION: Understanding human organ function and dysfunction requires detailed mapping of the anatomical and molecular architectures of cells and their organ-wide connectivity. Advances in imaging and molecular profiling technologies have greatly enriched our understanding of functional regions and the anatomical organization of cells and their molecular properties within human organs. However, we still lack technologies that allow us to capture multiscale multiomic properties of individual cells and their organ-wide connectivity in a holistic manner.

RATIONALE: We developed a scalable technology platform for simultaneous mapping of organ-wide structure and high-dimensional features, including molecular, morphological, and connectivity information, of cells acquired from the same tissue. The platform consists of a mechanical device enabling connectivity-preserving tissue slicing, a chemical technique for engineering tissue physicochemical properties to enable multiplexed multiscale molecular imaging, and a computational tool for single-cell projectome mapping. We fully integrated the

mechanical, chemical, and computational tools to enable highly multiplexed multiscale molecular phenotyping of human organ–scale tissues.

RESULTS: MEGAtome (mechanically enhanced great-size abrasion-free vibratome) enabled precision slicing of ultralarge biological systems while minimizing loss of connectivity information, thanks to the multi–degree of freedom (DOF) system optimizing the blade vibration control. MEGAtome slicing and light sheet imaging facilitated high-throughput molecular mapping of ultralarge-scale samples such as intact coronal human brain slabs and cohort-scale animal organ arrays. The integrated hydrogel-based tissue processing method called mELAST (magnifiable entangled link-augmented stretchable tissue-hydrogel) transformed biological tissues into elastic, transparent, and expandable hydrogels while preserving endogenous biomolecules and nanoscopic cellular architectures. Combined with a SWITCH (system-wide control of interaction time and kinetics of chemicals)–mediated rapid staining approach, mELAST enabled highly multiplexed multiscale imaging of intact human brain tissues. UNSLICE (unification of neighboring sliced-tissues via linkage of interconnected cut fiber endpoints) facilitated accurate interslab registration to reconstruct sliced tissue blocks at the single-fiber level using immunolabeled cell type–specific fibers as landmarks. The iterative nature of our strategy enabled the accuracy of connectivity mapping to continue to improve as we increased the dimensionality of the datasets. We applied the integrated technology platform to analyze human Alzheimer's disease (AD) pathology at multiple scales, unveiling diverse pathological features including differences in cell-type distributions, morphological features, neuronal fiber orientations, and chemical synapse distributions. Leveraging UNSLICE, we demonstrated scalable neural projection mapping at single-fiber resolution in human brains, revealing projection patterns of nerve fibers expressing pathological proteins.

CONCLUSION: Our technology platform enables scalable and fully integrated structural and molecular phenotyping of cells in human brain–scale tissues with unprecedented resolution and speed. We envision that this platform will empower holistic analysis of a large number of human and animal brains, thereby facilitating our understanding of interspecies homologies, population variances, and disease-specific features. Furthermore, our approach enables mapping of single-neuron projectomes and their integration with molecular expression profiles. This distinctive feature will allow us to elucidate the organization principles of neural circuitry and their disease-specific alterations in human brains, thus advancing our understanding of disease mechanisms. ■

Graphical Abstract:

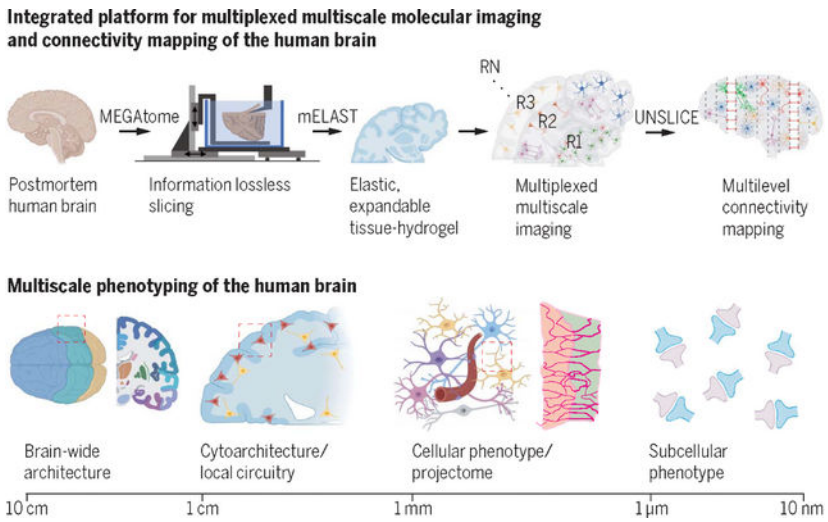

The integrated platform enables multiscale imaging and phenotyping of the human brain. The platform includes advanced mechanical, chemical, and computational technologies for multiscale imaging and connectivity mapping of the human brain. Using the platform, human brain hemispheres were MEGAtome-sliced and subsequently transformed into elastic and size-adjustable tissue-hydrogels for multiplexed multiscale imaging. The axon-level connectivity was restored using UNSLICE, revealing multidimensional features of human neuropathology.

A detailed mapping of the anatomical and molecular architectures of brain cells and their brain-wide connectivity is essential for understanding human brain function, the etiology of brain injuries, and the impact of brain diseases (1–3). Neuroimaging techniques, such as magnetic resonance imaging (MRI), functional MRI, and diffusion-weighted MRI, have increased our knowledge of the functional and structural organization of the human brain (4–8), but these methods fail to capture the fine structural, cellular, and molecular details owing to their limitations in spatial resolution (9, 10). Advanced histological approaches have provided a new window into local organization of cells but fail to capture brain-wide three-dimensional (3D) spatial information.

With the development of high-throughput single-cell and single-nucleus RNA sequencing (RNA-seq) technology (3, 11), many more cell types can be distinguished by their transcriptomic profiles, but these methods inherently limit the acquisition of spatial information and anatomical details of cells. Advances in spatial transcriptomics have enabled systematic analysis of cellular composition within tissue contexts (12). However, scaling these approaches to encompass entire human brains across many individuals remains challenging. Moreover, transcriptomic analysis alone cannot provide key information critical to understanding functional properties of cells, such as cellular morphology, connectivity, subcellular architectures, and protein posttranslational modifications and tracking. Therefore, there is a need to develop technologies that allow us to capture multiscale multiomic properties of individual cells and their brain-wide connectivity.

To address this challenge, we developed a fully integrated scalable technology platform to establish a 3D human brain cell atlas at subcellular resolution by simultaneously mapping

brain-wide structures and high-dimensional features (spatial, molecular, morphological, microenvironment, nanoscopic, and connectivity information) of cells acquired from the same whole human brains (Fig. 1). We accomplished this by seamlessly integrating new mechanical, chemical, and computational tools, enabling highly multiplexed multiscale 3D proteomic phenotyping of human brain tissues. We demonstrated its utility and scalability by processing the whole human brain hemispheres and investigating Alzheimer's disease (AD) pathology.

MEGAtome enables high-precision slicing of ultralarge biological tissues

State-of-the-art tissue clearing and processing methods (13–17) can render intact tissues optically transparent; however, the working distance (WD) for the objectives of existing microscope systems cannot cover the entire volume of human and large animal organs. In addition, residual variations in refractive index within cleared tissues cause loss of resolution, therefore mechanical sectioning is still required for imaging of large tissues.

Vibratomes are tools for sectioning soft tissues (18, 19). Conventional vibratomes (such as the Leica VT1200), however, are limited to small samples and often cause tissue damage. Furthermore, given their limited blade vibrating speed and large out-of-plane blade vibration, cut surfaces often suffer from abrasion, tears, and deformation.

To address these limitations, we developed a highly versatile vibratome, which we call MEGAtome (mechanically enhanced great-size abrasion-free vibratome), that enables ultraprecision slicing of a wide range of biological samples, from small organoids to intact human brain hemispheres and large arrays of animal organs (Fig. 2). MEGAtome enables high-frequency blade vibration with increased amplitude and low out-of-plane vibration displacement (fig. S1).

Analytical modeling and experimental data have shown that three elements benefit the precision and scalability of vibratome sectioning: (i) high blade vibration frequency, (ii) high vibration amplitude, and (iii) minimal out-of-plane blade displacement (20–22). To achieve these crucial elements, we designed a new blade vibration generation and control mechanism based on a multi–degree-of-freedom (multi-DOF) flexure series (Fig. 2, A to E).

The advantage of the multi-DOF design lies in its capability to operate at higher frequencies and increased amplitudes (Fig. 2F). Simulations and experiments (20) revealed amplified blade amplitude at the second resonant frequency, around 145 Hz (Fig. 2, G and H). MEGAtome's blade vibration amplitude linearly increases with its vibration input, reaching 3.4 mm peak-to-peak at 140 Hz, surpassing VT1200, which peaks at 2.4 mm peak-to-peak at 85 Hz (fig. S2). These results demonstrate that MEGAtome overcomes the trade-off between blade vibrating frequency and amplitude seen in typical single-DOF systems, achieving a 2.33 times higher blade vibrating speed than VT1200 at 1.65 times higher frequency.

To minimize the out-of-plane parasitic blade vibrations, we increased the system's out-of-plane stiffness with the flexure series design (Fig. 2, D, E, and I). To experimentally characterize this, we used high-precision capacitance probes to measure the out-of-plane displacement of the same blade mounted on both machines. The data indicate that the

MEGAtome exhibits lower out-of-plane vibration amplitudes compared with VT1200, despite operating at a much higher frequency (Fig. 2J).

It is worth noting that MEGAtome is unsuitable for sectioning hard samples, such as bone, paraffin-embedded, or frozen samples, owing to their high sample resistance, which disrupts blade vibration accuracy. However, MEGAtome excels in sectioning (i) soft tissues (fresh or chemically fixed or expanded), (ii) dense and highly myelinated tissues (human brainstem and spinal cord), and (iii) heterogeneous samples (human organs with connective tissues and embedded blood vessels) (figs. S1 and S3).

Next, we compared the precision of MEGAtome and VT1200 by slicing large human cerebellum tissues (36 mm by 45 mm by 20 mm) and measuring their surface profiles (Fig. 2K). MEGAtome produced intact slices with excellent surface evenness, preserving fine tissue architectures, whereas VT1200 generated highly uneven sections and caused severe damage to the cerebellar gyri and sulcus structures.

To confirm MEGAtome's information-preserving tissue slicing, we compared the distribution pattern of NFH+ (neurofilament heavy chain) fibers from adjacent human spinal cord sections (Fig. 2L) and the fiber connectivity and morphology of neurons from a PV-Cre MORF (mononucleotide repeat frameshift) mouse brain (23, 24) before and after MEGAtome slicing (Fig. 2M). Single-fiber resolution matching at cross sections indicates that MEGAtome slicing caused no damage or loss of fiber connectivity information.

Whole-mount slicing and imaging of large-scale tissue samples

Mechanical slicing is necessary to image large samples, such as human organs. Minimizing the number of dissected tissue blocks from large samples is advantageous, as it can drastically reduce human labor, cost, and information loss. For instance, whole-mount sectioning of an entire human brain hemisphere into intact thick coronal slabs is highly desirable, as slicing the same brain into cube-shaped blocks results in thousands of additional pieces. To whole-mount the human brain hemisphere securely for repeated slicing, we first developed a protocol to embed and chemically cross-link the brain in a hydrogel (Fig. 3A). We demonstrated that MEGAtome successfully sliced the whole-mounted human brain hemisphere and generated 40 consecutive 4-mm-thick slabs within 8 hours (Fig. 3B, fig. S4, and movie S1).

For imaging large slabs, we developed a multicolor inverted axially swept light-sheet fluorescence microscope, which we call MegaSPIM (Fig. 3C). MegaSPIM can capture multiscale data with objectives ranging from 2× to 25×, providing near-isotropic resolution and voxel sizes (fig. S5 and table S1). MegaSPIM is equipped with a continuous wavelength, multicolor laser source operating at 405, 488, 561, 647, and 785 nm. Custom-designed stages can accommodate tissue dimensions of up to 180 mm by 380 mm, enabling single-cell–resolution imaging of an expanded coronal human brain hemi slab (Fig. 4I, i).

Using MegaSPIM, we demonstrated high-throughput cellular-resolution imaging of a whole human brain hemisphere (Fig. 3, D and E). Figure 3D shows a SHIELD-cleared 4-mm-thick coronal human brain slab and annotation of subregions. Following staining with anti-NeuN

(neuronal nuclear protein) antibodies, we completed imaging of the entire slab in 6 hours, capturing the 3D distribution of NeuN+ neurons (Fig. 3E). Using a single MegaSPIM, a whole brain hemisphere can be imaged at single-cell resolution in ~100 hours.

Recent large-scale animal studies have greatly increased the need for high-throughput and cost-effective array-based imaging of tissues (25, 26). However, current approaches involve manual handling of individual samples, limiting throughput, increasing labor, and introducing sample-to-sample variations. To address this challenge, we developed a protocol to create high-density sample arrays compatible with MEGAtome for high-throughput processing and imaging of various biological samples (Fig. 3F and fig. S6). The protocol ensures that each sample is positioned in the same orientation with minimal spacing to maximize slicing and imaging efficiency. With this protocol, we demonstrated imaging of NeuN+ cells in mouse (whole brain slabs, 7 by 5) and marmoset (hemisphere brain slabs, 3 by 2) tissue arrays within 4 hours (Fig. 3G).

mELAST enables multiplexed multiscale imaging of large-scale tissues

Tissue transformation into a macromolecule-permeable and optically transparent hydrogel is a proven approach to investigate complex 3D biological systems (13). CLARITY (14), which hybridizes tissues with a synthetic polymer hydrogel, facilitates holistic imaging of intact tissues. Tissue expansion strategies (27–29) enable super-resolution imaging by imparting superabsorbent properties to tissue-hydrogel hybrids. Transmuting thick tissues into elastic materials using a polymer hydrogel with many slip links enables rapid probe transport (30). Nevertheless, an integrated technology enabling multiplexed multiscale imaging of the large-scale human brain is still lacking.

To tackle this challenge, we developed a tissue processing platform that we call mELAST (magnifiable entangled link-augmented stretchable tissue-hydrogel) by integrating SHIELD (31), SWITCH (32), MAP (33), and ELAST (30) technologies (Fig. 4). SHIELD (31) ensures permanent protein preservation during iterative staining, imaging, and destaining cycles. After SHIELD, mELAST transforms tissues into an elastic, thermochemically stable, and reversibly expandable tissue-hydrogel hybrid by means of in situ polymerization and subsequent postprocessing (Fig. 4, A and B, and figs. S7 and S8) (30, 33). We achieved 4.5-fold linear expansion in water while maintaining elasticity, integrity, and high durability of the tissue-hydrogel (Fig. 4C). mELAST successfully preserved protein epitopes (fig. S9 and table S2), and no structural or molecular information was lost during periodic compression or tissue expansion (fig. S10). The mELAST protocol is highly scalable and universally applicable even for entire coronal human brain slabs (Fig. 4A) and other species and organs without further optimization (figs. S7C and S11).

Autofluorescence materials in biological tissues, such as lipofuscin (34), can degrade signal and image quality during data acquisition. To address this issue, we built a photobleaching device for uniform photobleaching of autofluorescence from human brain (Fig. 4D). This approach substantially reduced tissue autofluorescence and improved signal-to-noise ratio (SNR) during data acquisition (Fig. 4, E and F, and fig. S12).

To achieve rapid, uniform, and cost-effective immunostaining, we developed a SWITCH-pumping method able to control reaction kinetics through SWITCH (32) during the rapid probe delivery by mechanical thinning (30). A custom-designed pump enabled highly reproducible mechanical thinning of large-scale tissues (Fig. 4G). The pump accelerates antibody delivery by reducing the characteristic tissue thickness and creating convective flow through nanopores within tissue-hydrogel by cyclic mechanical compression (Fig. 4H). During pumping-staining, we modulate antibody-antigen binding reactions using a SWITCH-staining buffer (fig. S13A). The SWITCH-pumping method drastically reduces the amount of antibodies required for staining large tissue volume while improving the staining uniformity, even for high-copy-number targets, such as parvalbumin (PV), neurofilament heavy chain (NFH), and phosphorylated neurofilament proteins (pNFP) (fig. S13, B and C). Automated pumps of various sizes ensure scalable tissue labeling (fig. S14).

mELAST with SWITCH-pumping enables multiscale molecular imaging of large human brain tissues (Fig. 4I). We achieved completely uniform staining of an mELAST-processed whole coronal human brain hemisphere slab with nuclear dye (YOYO-1) and primary antibodies within 12 hours, without any signal gradients in the entire tissue volume. Multiscale information was successfully acquired from the threefold linearly expanded tissue-hydrogel, including brain-wide structure, connection pathway, spatial cell distribution, and neuronal morphology (Fig. 4I, i to iv, and movies S2 and S3).

Multiplexed imaging allows for detailed analyses of cell types in tissues overcoming the spectral limitations of conventional fluorescence microscopy (35). With mELAST, we achieved highly multiplexed labeling and imaging of volumetric human brain tissues (Fig. 4J). After each round of staining and imaging, tissue underwent complete antibody elution and was then restained with the next set of antibodies. The universal applicability of our method enabled uniform staining of thick tissues with most antibodies under identical conditions, without additional optimization. The structural stability of the mELAST tissue-hydrogel allowed the samples to withstand extreme mechanical stresses (~60,000 cycles of fourfold compression) without damage. After completing seven rounds, we co-registered the multiround datasets at single-cell resolution using a computational algorithm, simultaneously mapping 11 major neuronal and non-neuronal markers in 3D (Fig. 4J and figs. S15 to S17). Taken together, mELAST facilitates large-scale tissue processing, multiplexed molecular staining with a single protocol, and volumetric imaging across various scales.

Multiscale interrogation of human brain tissues in Alzheimer's disease

We applied mELAST for interrogating the molecular and structural details of human brain tissues derived from two donors (Figs. 5 and 6): Donor 1 was a nondemented control (a 61-year-old female), and donor 2 had Alzheimer's disease (AD) dementia (an 88-year-old female). We sliced the two donor hemibrains using MEGAtome and obtained intact coronal slabs at the same neuroanatomical level.

After SHIELD-clearing, the slabs were stained with nuclear dyes (YOYO-1) and anti-NeuN antibodies and imaged at single-cell resolution (Fig. 5A). Nuclear staining enables detection

of all nuclei for co-registration of multiround datasets at single-cell resolution. The pan-neuronal marker NeuN facilitates cytoarchitectural parcellations. A custom-built algorithm was used for 3D-segmentation of brain subregions in the volumetric datasets, followed by cell counting and density calculation (Fig. 5B).

Using our 3D cell phenotyping algorithm, NeuN+ cells were automatically detected in both slabs (Fig. 5A and table S3, detection accuracy = 95.1%) (36). Cellular profiling of the entire slabs resulted in a total of 7,464,727 NeuN+ cells in control and 2,890,858 NeuN+ cells in AD. The NeuN+ cell density was 46.5% lower in AD compared with control ($13.0 \times 10^3/mm^3$ versus $24.3 \times 10^3/mm^3$), a more severe loss than previous reports (22 to 40%) (37). In control, no regional differences were observed in NeuN+ cell density, whereas in AD, the NeuN+ cell density in cingulate gyrus (CgG) and orbital gyrus (OrG) was lower compared with other brain regions.

We further investigate cellular and molecular changes in the regions with high neuronal loss, orbitofrontal cortex (OFC) from OrG (table S4). The OFC is a frontal cortex region known for its role in high-order cognition tasks such as decision-making, where connectivity is impaired in later stages of AD (38–40). We performed multiround immunostaining and multiscale imaging of the mELAST-processed tissues, using a set of neuronal subtype markers [PV, calretinin (CR), neuropeptide-Y (NPY), and somatostatin (SST)], glia subtype markers [ionized calcium-binding adaptor molecule 1 (Iba1) for microglia, glial fibrillary acidic protein (GFAP) for activated astrocytes, and myelin basic protein (MBP) for oligodendrocytes], a structural panaxonal marker [phosphorylated neurofilament proteins (pNFP)], pathogenic protein markers [amyloid beta (Ab) and phosphorylated tau (pTau)], an endothelial cell marker [cluster of differentiation 31 (CD31/PECAM-1)], and synaptic markers [synapsin I and II (Syn I/II) and postsynaptic density protein 95 (PSD-95)] to map key molecules associated with cellular, structural, connectivity, and pathological processes. The multichannel datasets were co-registered at single-cell resolution (Fig. 5, C and D; figs. S15 and S18; and movies S4 and S5).

We observed distinct distribution patterns of the pathology-associated proteins [amyloid-β (Aβ) and phosphorylated tau (pTau)] and astrocytes (GFAP) in AD compared with control (Fig. 5, C to E, and movie S6). In AD, Aβ senile plaques enveloping pTau+ neurofibrillary tangles were densely distributed throughout the entire cortical area, as is well known (41), contrasting with primarily layer III localization in control with very few pTau+ tangles. In control, processes from interlaminar astrocytes at the pial surface were broadly observed to extend into layers III and IV. However, the density of interlaminar astrocytes was lower in AD, and their processes extended only into the boundary of layers II and III, consistent with previous observations (42). The reduction of their density and reach may point to compromised structural stability in AD (43). We also observed an abnormal increase in the number of astrocytes in AD as a result of neuroinflammation (44, 45).

Next, we investigated how axonal projection patterns are altered in AD by characterizing pNFP+ fiber orientations (Fig. 5, F and G, and fig. S19). In control, we observed large populations of pNFP+ fibers oriented parallel, orthogonally, and obliquely to the pial surface, whereas in AD these fibers were primarily orthogonally oriented, consistent with

previous findings (46). In control, orthogonally oriented fibers were present in all cortical layers, whereas obliquely and parallel oriented fibers were primarily found in layers I and III to V. In AD, all six layers exhibited similar distributions of orthogonally oriented fibers, indicating a shift in pNFP+ axonal orientation.

Spatial organization of different cell types was studied by measuring the density of nuclei and each neuron subtype (Fig. 5H, tables S5 to S7, and fig. S20). Nuclei density measurement showed a lower total cell density in AD compared with control. CR+ (in layers I to III), PV+ (in layers III to V), and CR+/PV+ (in layers I to III) interneurons displayed lower density in AD, a pattern potentially associated with neurodegeneration, impaired homeostasis, and calcium-based signaling, consistent with the literature (47, 48). Additionally, the Iba1+ microglia density was higher (1.81 times on average) across all cortical layers in AD compared with control (Fig. 5H), suggesting increased immune activation.

We investigated the relationship between various cell types, pNFP, and neurofibrillary tangles (NFTs) (Fig. 5I and table S8). NFTs, a hallmark of AD, are abnormal accumulations of pTau, neurofilaments, and other cytoskeleton proteins, causing neuronal dysfunction and death (46, 49–51). We used anti-pNFP antibodies to visualize phosphorylated epitopes on medium and heavy subunits of neurofilament proteins. Unlike control, in which no pNFP+ cell bodies were found, many pNFP+ cell bodies were detected in AD. The pNFP+ cells were concentrated in layers III and V (77.1%), the main residence sites for pyramidal cells. No colocalization between pNFP and the interneuronal markers (PV, CR, NPY, and SST) was observed, consistent with reports for selective vulnerability of pyramidal neurons in AD (tables S6 and S7) (50, 51). Most NFT-containing neurons (82.6%) were pNFP+ (pTau+/pNFP+, 54.2%; pTau−/pNFP+, 28.4%) and only 17.4% were pTau+/pNFP− cells, implying that phosphorylation of neurofilament proteins and their accumulation in specific neuronal populations may precede perikaryal pTau aggregation (52).

To further investigate subcellular architectures, we performed high-resolution imaging of layer III, where Aβ plaques showed high accumulation in both cases (Fig. 6A and movie S7). Most Aβ plaques in AD were neuritic, dense-core plaques known to be closely associated with neuronal and synaptic loss (53), whereas Aβ plaques in control were diffuse forms (Fig. 6, A and B).

As previously observed (54), most Iba1+ microglia were in the highly-branched, ramified form (77.6%), but microglia in the reactive form were observed inside and around diffuse Aβ plaques (22.4%) in control (Fig. 6F, left). In AD, most microglia (79.6%) were reactive, showing that the OFC may exhibit a greater difference in the ratio of ramified/reactive microglia compared to other cortex regions analyzed in literature (55). Additionally, rod-shaped microglia observed in numerous pathological conditions were identified in AD (12.2%) but not in control (0%). The elongated body axis of all rod-shaped microglia found in the region of interest were oriented perpendicular to the pial surface (fig. S21) (56).

A comparative morphological evaluation of GFAP+ astrocytes in layer III was conducted (Fig. 6, A and C). In control, GFAP+ structures were predominantly composed of long,

unbranched processes of interlaminar astrocytes located near the pial surface. In AD, these long processes were not detected. Instead, most GFAP+ cells were protoplasmic astrocytes in reactive form, with 31.9-fold higher density in AD versus control (Fig. 6F, right) (42–45, 57).

Dendrite morphology analysis of CR+ interneurons revealed differences in arborization patterns between AD and control (Fig. 6, A, D, and G) (58). Whereas the majority of CR+ cells in control showed a multipolar dendrite morphology with complex branching patterns (69.7%), bipolar or bitufted neurons with less branching were more numerous in AD (61.5%). Furthermore, we noticed that some bipolar or bitufted CR+ neurons in AD had peculiar shapes, with their cell bodies in very close contact with each other.

In AD, pTau+/pNFP+ fibers were abundant, indicating the accumulation of pTau in axons, whereas in control, only a few pretangles and neuropil threads were observed (Fig. 6, A and E). Whereas pTau−/pNFP+ axons in control were thin (thickness = 1.94 ± 0.64 μm) and largely myelinated, many of the pTau+/pNFP+ axons inside the Aβ plaques in AD appeared swollen (3.89 ± 2.00 μm) and demyelinated (Fig. 6, H to K) (59, 60). In AD, MBP+ pixel density inside the Aβ plaques was one-tenth that outside the plaques, whereas in control, we observed only 38.8% reduction in MBP pixel density (71.3 ± 6.9 outside the plaques versus 43.6 ± 5.0 inside the plaques) (Fig. 6I) (61, 62).

Finally, to investigate whether synaptic structures are affected in AD, we performed super-resolution imaging of the same region in both tissues that were linearly expanded fourfold (Fig. 6, L and M; table S4; and movie S8). We assessed pre- and postsynaptic density (Syn I/II and PSD-95) inside and outside the Aβ plaques. Whereas the synaptic density within the diffuse Aβ plaques was similar to that outside of the plaques in control, we found a 90% decrease in Syn I/II density inside the neuritic Aβ plaques compared with that outside (63–65). The synapse density outside of the Aβ plaques in AD and control was similar. Collectively, these phenotyping results demonstrate that our mELAST technology enables extraction of pathological changes at multiscale from the same human samples.

UNSLICE enables multilevel connectivity mapping of the human brain

A computational pipeline capable of registering multiple slabs with single-fiber accuracy is required for mapping the 3D neural connectivity across sliced tissues (fig. S22). Current computational reconstruction methods often work with thin, undeformed, or laterally small tissue sections (66–69), making them unapplicable for large, heavily processed human brain slab–scale images. Other methods for large mammalian tissue have not achieved accurate reconstruction of densely immunolabeled neurites in human brain tissue at single-fiber resolution (70).

To accomplish accurate multiscale reconstruction of thick tissue volumes, we developed a computational pipeline called UNSLICE (unification of neighboring sliced-tissues via linkage of interconnected cut fiber endpoints), which accurately aligns anatomical features at macro-, meso- (blood vessels), and micro-scale (axons) levels (Fig. 7A). Intensity or feature-based registration methods [such as Harris corner detector (32)] used for 2D image

registration do not scale to interslab registration of large, thick, and highly processed tissue owing to deformation, requiring more-relevant and -reliable features.

To this end, UNSLICE takes advantage of fluorescent labeling of vasculature to match blood vessel endpoints at the cut surfaces to define a smooth deformation field. Blood vessels are ideal for interslab registration because of their long-range continuity and connectivity; high SNR staining profile; and dense, ubiquitous distribution throughout the brain (71, 72). By ensuring vessel connectivity across connectivity across consecutive tissue slabs, we achieve effective macroscopic and mesoscopic alignment between multiple slabs.

UNSLICE uses the following semiautomated processes (Fig. 7A and figs. S23 and S24): step 1, image preprocessing; step 2, surface detection; step 3, surface flattening (73); step 4, identifying matching “anchor points”; step 5, detecting, segmenting, and skeletonizing surface vessel endpoints (74); step 6, matching endpoints between the two surfaces; step 7, applying deformation to fuse the volumes; step 8, annotating additional endpoints in the transformed frame; and step 9, iteratively repeating steps 7 and 8 for progressively improved connectivity alignment at vasculature resolution. Furthermore, by applying this method to image channels containing axonal or neural fiber information, we can fine-tune the vasculature-scale registration to restore axon connectivity across sliced tissue slabs.

To demonstrate UNSLICE’s capability for single capillary and axonal-scale interslab registration, we applied it to two different types of datasets, each with “ground truth”: (i) PV-Cre MORF mouse tissue (Fig. 7B and movie S9) (23, 24) and (ii) NFH-labeled human brain tissue (fig. S25A). We quantified the accuracy of interslab registration (Fig. 7C and fig. S25B) and computed the distance between perfectly matched corresponding fiber endpoints in both the ground truth and UNSLICE’d datasets: an average error of 1.29 μm (PV+ neurites) and 1.13 μm (NFH+ neurofibers). The results demonstrated the robustness of UNSLICE across varying tissue types, stains, objectives, and datasets, successfully restoring connectivity of fibers through the cut surfaces.

We applied UNSLICE to consecutive image volumes from millimeter-thick coronal human brain hemisphere slabs (Fig. 7D, fig. S26, and movie S10) and 26 human pons slabs (Fig. 7E and figs. S27 and S28). The computational flattening step proved especially advantageous in this dataset owing to the substantially larger lateral area and irregular shape of the multiple slabs (fig. S24). By combining manually defined correspondences for warp initialization with automated vessel endpoint matching in an iterative and parallelized fashion, the user has flexibility in choosing the level of precision. The successful application of UNSLICE showcases the scalability of our pipeline for proteomic and projectomic analysis of large-scale human organ tissue.

Axonal projectome mapping and pathological analysis of the human brain

Vasculature alone is not sufficiently dense to achieve the single-axon resolution registration required for projectome mapping and axon tracing. After vessel-resolution registration, the fiber endpoints of other cell type markers (GFAP, PV, and NFH) were used to refine the registration results (Fig. 8A). This refinement enabled multichannel spatial reconstruction

of multiple slabs at single-fiber scale (fig. S29 and movie S11). Additionally, because UNSLICE's topographic feature matching and outlier removal steps were designed to tolerate both false negatives and positives in fiber endpoint detection, the same vesselness filter, segmentation, and skeletonization steps can be used for automated fiber endpoint detection, even with endpoint detection F1 scores in the 85 to 90% range (fig. S24).

Progressive improvement in the accuracy of individual NFH+ axon connectivity through the tissue sections was observed as additional landmarks from different cell type markers were incorporated (Fig. 8, B and C). This multistage registration approach also enhanced the connectivity of GFAP+ fibers. Specifically, the distribution of *x*- and *y*-axis NFH+ fiber connectivity error shrinks from a spread of 10 μm (in each lateral dimension) after lectin registration, to ~5 μm after PV/GFAP registration, and finally minimized to ~1 μm after NFH registration.

Automated and semiautomated neuron tracing and segmentation algorithms have been developed for analyzing high-resolution images of single neurons or sparsely labeled groups of neurons (75–77). Although these algorithms are suitable for tracing high-resolution, high-SNR, and sparsely labeled light microscopy images (such as electron microscopy images), high-accuracy tracing of densely packed axons in immunostained tissue volumes requires different features. Toward this end, we have developed a deep learning–based axon segmentation and tracing algorithm based on the 3D extension of U-Net architecture (Fig. 8D) (78). For end-to-end centerline detection, the algorithm uses a centerline-Dice (clDice) loss function (79, 80), allowing us to incorporate parameter-free skeletonization directly into the optimization process.

The UNSLICE and axon tracing algorithms enabled the reconstruction of AD human tissue blocks at multiple levels (Fig. 8E and movie S12). pTau+ fibers that traversed the tissue slab seams were reconnected, segmented, and traced (Fig. 8, F and G, and fig. S30). The orientation of the traced pTau+ fibers was analyzed throughout the whole reconstructed volume (Fig. 8, H and I). We found that most fibers were oriented in the direction corresponding to an azimuthal angle $\theta = 30°$ to 60° (with 0° corresponding to perfect alignment with the *z* axis and 90° corresponding to perfect alignment with the *xy* plane) and a polar angle $\varphi = -30°$ to 30°, corresponding to fibers aligned with the *x* axis. We estimated the orientation of the cortical column and compared our fiber orientation results to it. Qualitatively, the majority of pTau+ fibers were aligned parallel to the cortical column (Fig. 8J). These data demonstrate that our computational pipeline is capable of accurate, scalable connectivity mapping of human brain tissues.

Discussion

We have developed multiple technologies and seamlessly integrated them to establish a scalable platform for fully integrated anatomical and molecular phenotyping of cells in human-organ–scale tissues with unprecedented resolution and speed. MEGAtome realizes precision slicing of ultralarge tissues with minimal loss of information. Its multi-DOF design amplifies blade vibrating speed at high frequencies while minimizing the blade mechanical

errors. MEGAtome combined with a synergistic gelembedding protocol facilitates high-throughput imaging of ultralarge tissues, preserving connectivity information.

The expandability, compressibility, and chemical stability of the mELAST tissue-hydrogel enables multiplexed, multiscale volumetric imaging of human brain tissues with negligible information loss. mELAST maximizes the utility of rare and highly valuable human clinical tissues and allows the resulting datasets to evolve continuously beyond the scope of individual studies, enabling the community to jointly and continuously probe the same samples.

Multiscale phenotyping of the two human brains (the control and AD cases) using mELAST uncovered apparent pathological features in AD tissue (Figs. 5 and 6), including neuronal loss (37, 50, 51), tauopathy (41, 52), β-amyloidosis (53), astrogliosis (42–45), microgliosis (54–56), axonopathy (59, 60), myelinopathy (61, 62), and synaptopathy (63–65), consistent with literature. We could simultaneously capture protein expression, cellular morphology, neural projection, and synapse distribution information from the same brain tissues, a highly desirable feature given interindividual variation (81). pTau-associated axonal swelling, correlated with severe axonopathy, demyelination and synapse loss in regions surrounded by neuritic Aβ plaques, supports neuroimaging studies that suggest severe damage to the connectivity of the OFC in the late stages of AD (39).

Mapping neural connectivity in the human brain remains challenging, as current interrogation techniques (such as viral labeling) are restricted to experimental animal systems (70, 82). We demonstrated reconstruction of interslab axonal connectivity in human brain tissue. The iterative nature of our analytical strategy ensures that the accuracy of tracing continues to improve as we increase the dimensionality of the datasets by adding additional rounds of fiber-resolution images. The comprehensive circuit mapping enabled by this platform will enable the identification of noncanonical connections, enhancing our understanding of human brain circuitry.

To enhance axon-level stitching accuracy and determine each axon’s cell type, incorporating more antibodies could be beneficial, as shown in Fig. 8, A to C. However, achieving axon-level multiround co-registration remains a complex challenge at this stage. Further development of single axon–level co-registration algorithms, possibly using the NFH staining in each imaging round, is warranted. Overall, our platform enables single-neuron reconstruction without relying on viral labeling, making it particularly advantageous for studies involving human and nonhuman primates where genetic labeling is not permitted. We envision that this scalable technology platform will advance our understanding of the human organ functions and disease mechanisms to spur development of new therapies.

Materials and methods summary

The postmortem human brain hemispheres were first embedded in a gel for mounting and then sliced using MEGAtome. We assessed the slicing quality by measuring the surface roughness with an optical surface profiler. The sliced human brain tissues underwent SHIELD processing and were hybridized with mELAST polymer hydrogel for permanent

protein preservation and transformation of them into transparent, elastic, and expandable materials. We then immunostained the engineered human brain tissues either passively or actively using a SWITCH-pumping method with antibodies and dyes. The tissues were imaged at multiple scales using a confocal microscope or MegaSPIM, with the use of various magnification objectives after optical clearing. We repeated the staining, imaging, and destaining processes in multiple rounds for image multiplexing. The imaging data were stitched together, postprocessed, and subjected to computational analyses, including brain subregion segmentation, cell and synapse counting, morphological reconstruction and classification, and analyses. The images from the sectioned and engineered tissues were reintegrated using UNSLICE based on the endpoint detection and matching at single axonal accuracy. The stitching accuracy of blood vessels and neurofibers in the UNSLICE'd images was evaluated, and their characteristics were analyzed through fiber tracing. Full materials and methods are available in supplementary materials.

Supplementary Material

Refer to Web version on PubMed Central for supplementary material.

ACKNOWLEDGMENTS

We thank the entire Chung laboratory for support and discussions. Resources that may help enable general users to establish the methodology are freely available online (http://www.chunglabresources.org). The cartoon in Fig. 1 was created with BioRender.com.

Funding:

K.C. was supported by the Burroughs Wellcome Fund Career Awards at the Scientific Interface, Searle Scholars Program, Packard Fellowship in Science and Engineering, NARSAD Young Investigator Award, and McKnight Foundation Technology Award. This work was supported by the JPB Foundation (PIIF and PNDRF to K.C.), NCSOFT Cultural Foundation, and NIH (1-DP2-ES027992, U01MH117072 to K.C.). J.P. was partially supported by the Institute for Basic Science (IBS-R026-D1 to J.P.). J.W. and J.P. were supported as Picower Fellows by The Picower Institute of Learning and Memory. W.G. was supported by the National Science Foundation Graduate Research Fellowship under grant 1122374 (to W.G.). M.P.F. was partially supported by NIA P50 AG005134 (to M.P.F.). C.D.K. was partially supported by NIH P30 AG066509 (to C.D.K.) and the Nancy and Buster Alvord endowment.

Data and materials availability:

The human brain microscopy image data from the SHIELD and mELAST tissues acquired using MegaSPIM for the BICCN (RRID:SCR_015820) by J.P. and colleagues can be accessed in the DANDI Archive (RRID:SCR_017571) under accession number DANDI:000108. Data may be accessed at https://dandiarchive.org/dandiset/000108 (84). Neuroglancer view of the data on DANDI: https://biccn.github.io/Quarterly_Submission_Receipts/000108-dashboard.html (the overlapped chunks in each slab are "stitched" using the rigid transform available with each chunk). All other datasets used in this paper are available upon request. Code used for the paper can be found in the following Github repositories: https://github.com/chunglabmit/spimstitch (post-acquisition preprocessing, such as illumination correction, tile stitching, and file conversion), https://github.com/chunglabmit/unslice (UNSLICE), and https://github.com/chunglabmit/multiround-alignment-ui (multiround image co-registration). The cell counting

code will be released upon institutional review for open-source. The axon tracing code will be released upon institutional review for open-source.

REFERENCES AND NOTES

1. Biswal BB et al. , Toward discovery science of human brain function. Proc. Natl. Acad. Sci. U.S.A. 107, 4734–4739 (2010). doi: 10.1073/pnas.0911855107 [PubMed: 20176931]
2. Bassett DS, Gazzaniga MS, Understanding complexity in the human brain. Trends Cogn. Sci. 15, 200–209 (2011). doi: 10.1016/j.tics.2011.03.006 [PubMed: 21497128]
3. Hawrylycz MJ et al. , An anatomically comprehensive atlas of the adult human brain transcriptome. Nature 489, 391–399 (2012). doi: 10.1038/nature11405 [PubMed: 22996553]
4. Glover P, Bowtell R, Medical imaging: MRI rides the wave. Nature 457, 971–972 (2009). doi: 10.1038/457971a [PubMed: 19225512]
5. Evans AC, Janke AL, Collins DL, Baillet S, Brain templates and atlases. Neuroimage 62, 911–922 (2012). doi: 10.1016/j.neuroimage.2012.01.024 [PubMed: 22248580]
6. Amunts K et al. , Interoperable atlases of the human brain. Neuroimage 99, 525–532 (2014). doi: 10.1016/j.neuroimage.2014.06.010 [PubMed: 24936682]
7. Fischl B, Sereno MI, Tootell RBH, Dale AM, High-resolution intersubject averaging and a coordinate system for the cortical surface. Hum. Brain Mapp. 8, 272–284 (1999). doi: 10.1002/(SICI)1097-0193(1999)8:4<272::AID-HBM10>3.0.CO;2-4 [PubMed: 10619420]
8. Fischl B, Dale AM, Measuring the thickness of the human cerebral cortex from magnetic resonance images. Proc. Natl. Acad. Sci. U.S.A. 97, 11050–11055 (2000). doi: 10.1073/pnas.200033797 [PubMed: 10984517]
9. Amunts K, Zilles K, Architectonic mapping of the human brain beyond Brodmann. Neuron 88, 1086–1107 (2015). doi: 10.1016/j.neuron.2015.12.001 [PubMed: 26687219]
10. Caspers S, Eickhoff SB, Zilles K, Amunts K, Microstructural grey matter parcellation and its relevance for connectome analyses. Neuroimage 80, 18–26 (2013). doi: 10.1016/j.neuroimage.2013.04.003 [PubMed: 23571419]
11. Miller JA et al. , Transcriptional landscape of the prenatal human brain. Nature 508, 199–206 (2014). doi: 10.1038/nature13185 [PubMed: 24695229]
12. Chen KH, Boettiger AN, Moffitt JR, Wang S, Zhuang X, Spatially resolved, highly multiplexed RNA profiling in single cells. Science 348, aaa6090 (2015). doi: 10.1126/science.aaa6090 [PubMed: 25858977]
13. Choi SW, Guan W, Chung K, Basic principles of hydrogel-based tissue transformation technologies and their applications. Cell 184, 4115–4136 (2021). doi: 10.1016/j.cell.2021.07.009 [PubMed: 34358468]
14. Chung K et al. , Structural and molecular interrogation of intact biological systems. Nature 497, 332–337 (2013). doi: 10.1038/nature12107 [PubMed: 23575631]
15. Susaki EA et al. , Whole-brain imaging with single-cell resolution using chemical cocktails and computational analysis. Cell 157, 726–739 (2014). doi: 10.1016/j.cell.2014.03.042 [PubMed: 24746791]
16. Mai H et al. , Whole-body cellular mapping in mouse using standard IgG antibodies. Nat. Biotechnol. 42, 617–627 (2024). doi: 10.1038/s41587-023-01846-0 [PubMed: 37430076]
17. Renier N et al. , iDISCO: A simple, rapid method to immunolabel large tissue samples for volume imaging. Cell 159, 896–910 (2014). doi: 10.1016/j.cell.2014.10.010 [PubMed: 25417164]
18. Li W, Shepherd DET, Espino DM, Dynamic mechanical characterization and viscoelastic modeling of bovine brain tissue. J. Mech. Behav. Biomed. Mater. 114, 104204 (2021). doi: 10.1016/j.jmbbm.2020.104204 [PubMed: 33218929]
19. Rashid B, Destrade M, Gilchrist MD, Mechanical characterization of brain tissue in compression at dynamic strain rates. J. Mech. Behav. Biomed. Mater. 10, 23–38 (2012). doi: 10.1016/j.jmbbm.2012.01.022 [PubMed: 22520416]
20. Wang J, Li C, Chen SC, Sectioning soft materials with an oscillating blade. Precis. Eng. 56, 96–100 (2019). doi: 10.1016/j.precisioneng.2018.11.002

21. Mora S, Pomeau Y, Cutting and slicing weak solids. Phys. Rev. Lett. 125, 038002 (2020). doi: 10.1103/PhysRevLett.125.038002 [PubMed: 32745431]
22. Reyssat E, Tallinen T, Le Merrer M, Mahadevan L, Slicing softly with shear. Phys. Rev. Lett. 109, 244301 (2012). doi: 10.1103/PhysRevLett.109.244301 [PubMed: 23368324]
23. Yun DH et al. , Ultrafast immunostaining of organ-scale tissues for scalable proteomic phenotyping. bioRxiv 660373 [Preprint] (2019); 10.1101/660373.
24. Veldman MB et al. , Brainwide genetic sparse cell labeling to illuminate the morphology of neurons and glia with Cre-dependent MORF mice. Neuron 108, 111–127.e6 (2020). doi: 10.1016/j.neuron.2020.07.019 [PubMed: 32795398]
25. Glaser AK et al. , A hybrid open-top light-sheet microscope for versatile multi-scale imaging of cleared tissues. Nat. Methods 19, 613–619 (2022). doi: 10.1038/s41592-022-01468-5 [PubMed: 35545715]
26. Beachley VZ et al. , Tissue matrix arrays for high-throughput screening and systems analysis of cell function. Nat. Methods 12, 1197–1204 (2015). doi: 10.1038/nmeth.3619 [PubMed: 26480475]
27. Chen F, Tillberg PW, Boyden ES, Expansion microscopy. Science 347, 543–548 (2015). doi: 10.1126/science.1260088 [PubMed: 25592419]
28. Wang G, Moffitt JR, Zhuang X, Multiplexed imaging of high-density libraries of RNAs with MERFISH and expansion microscopy. Sci. Rep. 8, 4847 (2018). doi: 10.1038/s41598-018-22297-7 [PubMed: 29555914]
29. Park H-E et al. , Scalable and isotropic expansion of tissues with simply tunable expansion ratio. Adv. Sci. 6, 1901673 (2019). doi: 10.1002/advs.201901673
30. Ku T et al. , Elasticizing tissues for reversible shape transformation and accelerated molecular labeling. Nat. Methods 17, 609–613 (2020). doi: 10.1038/s41592-020-0823-y [PubMed: 32424271]
31. Park YG et al. , Protection of tissue physicochemical properties using polyfunctional crosslinkers. Nat. Biotechnol. 37, 73–83 (2018). doi: 10.1038/nbt.4281
32. Murray E et al. , Simple, scalable proteomic imaging for high-dimensional profiling of intact systems. Cell 163, 1500–1514 (2015). doi: 10.1016/j.cell.2015.11.025 [PubMed: 26638076]
33. Ku T et al. , Multiplexed and scalable super-resolution imaging of three-dimensional protein localization in size-adjustable tissues. Nat. Biotechnol. 34, 973–981 (2016). doi: 10.1038/nbt.3641 [PubMed: 27454740]
34. Schnell SA, Staines WA, Wessendorf MW, Reduction of lipofuscin-like autofluorescence in fluorescently labeled tissue. J. Histochem. Cytochem. 47, 719–730 (1999). doi: 10.1177/002215549904700601 [PubMed: 10330448]
35. Hickey JW et al. , Spatial mapping of protein composition and tissue organization: A primer for multiplexed antibody-based imaging. Nat. Methods 19, 284–295 (2022). doi: 10.1038/s41592-021-01316-y [PubMed: 34811556]
36. Albanese A et al. , Multiscale 3D phenotyping of human cerebral organoids. Sci. Rep. 10, 21487 (2020). doi: 10.1038/s41598-020-78130-7 [PubMed: 33293587]
37. Coleman PD, Flood DG, Neuron numbers and dendritic extent in normal aging and Alzheimer's disease. Neurobiol. Aging 8, 521–545 (1987). doi: 10.1016/0197-4580(87)90127-8 [PubMed: 3323927]
38. Van Hoesen GW, Parvizi J, Chu CC, Orbitofrontal cortex pathology in Alzheimer's disease. Cereb. Cortex 10, 243–251 (2000). doi: 10.1093/cercor/10.3.243 [PubMed: 10731219]
39. Tekin S, Cummings JL, Frontal–subcortical neuronal circuits and clinical neuropsychiatry: An update. J. Psychosom. Res. 53, 647–654 (2002). doi: 10.1016/S0022-3999(02)00428-2 [PubMed: 12169339]
40. Bechara A, Damasio H, Damasio AR, Emotion, decision making and the orbitofrontal cortex. Cereb. Cortex 10, 295–307 (2000). doi: 10.1093/cercor/10.3.295 [PubMed: 10731224]
41. Bloom GS, Amyloid-β and tau: The trigger and bullet in Alzheimer disease pathogenesis. JAMA Neurol. 71, 505–508 (2014). doi: 10.1001/jamaneurol.2013.5847 [PubMed: 24493463]
42. Colombo JA, Quinn B, Puissant V, Disruption of astroglial interlaminar processes in Alzheimer's disease. Brain Res. Bull. 58, 235–242 (2002). doi: 10.1016/S0361-9230(02)00785-2 [PubMed: 12127023]

43. Vasile F, Dossi E, Rouach N, Human astrocytes: Structure and functions in the healthy brain. Brain Struct. Funct. 222, 2017–2029 (2017). doi: 10.1007/s00429-017-1383-5 [PubMed: 28280934]
44. Colombo E, Farina C, Astrocytes: Key regulators of neuroinflammation. Trends Immunol. 37, 608–620 (2016). doi: 10.1016/j.it.2016.06.006 [PubMed: 27443914]
45. Simpson JE et al. , Astrocyte phenotype in relation to Alzheimer-type pathology in the ageing brain. Neurobiol. Aging 31, 578–590 (2010). doi: 10.1016/j.neurobiolaging.2008.05.015 [PubMed: 18586353]
46. Masliah E et al. , An antibody against phosphorylated neurofilaments identifies a subset of damaged association axons in Alzheimer's disease. Am. J. Pathol. 142, 871–882 (1993). [PubMed: 8456946]
47. Zallo F, Gardenal E, Verkhratsky A, Rodríguez JJ, Loss of calretinin and parvalbumin positive interneurones in the hippocampal CA1 of aged Alzheimer's disease mice. Neurosci. Lett. 681, 19–25 (2018). doi: 10.1016/j.neulet.2018.05.027 [PubMed: 29782955]
48. Ruden JB, Dugan LL, Konradi C, Parvalbumin interneuron vulnerability and brain disorders. Neuropsychopharmacology 46, 279–287 (2021). doi: 10.1038/s41386-020-0778-9 [PubMed: 32722660]
49. Liu Q et al. , Neurofilament proteins in neurodegenerative diseases. Cell. Mol. Life Sci. 61, 3057–3075 (2004). doi: 10.1007/s00018-004-4268-8 [PubMed: 15583867]
50. Bussière T et al. , Progressive degeneration of nonphosphorylated neurofilament protein-enriched pyramidal neurons predicts cognitive impairment in Alzheimer's disease: Stereologic analysis of prefrontal cortex area 9. J. Comp. Neurol. 463, 281–302 (2003). doi: 10.1002/cne.10760 [PubMed: 12820162]
51. Bussière T et al. , Stereologic analysis of neurofibrillary tangle formation in prefrontal cortex area 9 in aging and Alzheimer's disease. Neuroscience 117, 577–592 (2003). doi: 10.1016/S0306-4522(02)00942-9 [PubMed: 12617964]
52. Serrano-Pozo A, Frosch MP, Masliah E, Hyman BT, Neuropathological alterations in Alzheimer disease. Cold Spring Harb. Perspect. Med. 1, a006189 (2011). doi: 10.1101/cshperspect.a006189 [PubMed: 22229116]
53. DeTure MA, Dickson DW, The neuropathological diagnosis of Alzheimer's disease. Mol. Neurodegener. 14, 32 (2019). doi: 10.1186/s13024-019-0333-5 [PubMed: 31375134]
54. Nelson PT, Soma LA, Lavi E, Microglia in diseases of the central nervous system. Ann. Med. 34, 491–500 (2002). doi: 10.1080/078538902321117698 [PubMed: 12553488]
55. Paasila PJ, Davies DS, Kril JJ, Goldsbury C, Sutherland GT, The relationship between the morphological subtypes of microglia and Alzheimer's disease neuropathology. Brain Pathol. 29, 726–740 (2019). doi: 10.1111/bpa.12717 [PubMed: 30803086]
56. Taylor SE, Morganti-Kossmann C, Lifshitz J, Ziebell JM, Rod microglia: A morphological definition. PLOS ONE 9, e97096 (2014). doi: 10.1371/journal.pone.0097096 [PubMed: 24830807]
57. Colombo JA, Reisin HD, Interlaminar astroglia of the cerebral cortex: A marker of the primate brain. Brain Res. 1006, 126–131 (2004). doi: 10.1016/j.brainres.2004.02.003 [PubMed: 15047031]
58. Petilla Interneuron Nomenclature Group, Petilla terminology: Nomenclature of features of GABAergic interneurons of the cerebral cortex. Nat. Rev. Neurosci. 9, 557–568 (2008). doi: 10.1038/nrn2402 [PubMed: 18568015]
59. Griffa A, Baumann PS, Thiran JP, Hagmann P, Structural connectomics in brain diseases. Neuroimage 80, 515–526 (2013). doi: 10.1016/j.neuroimage.2013.04.056 [PubMed: 23623973]
60. Stokin GB et al. , Axonopathy and transport deficits early in the pathogenesis of Alzheimer's disease. Science 307, 1282–1288 (2005). doi: 10.1126/science.1105681 [PubMed: 15731448]
61. Zhang X et al. , Oligodendroglial glycolytic stress triggers inflammasome activation and neuropathology in Alzheimer's disease. Sci. Adv. 6, eabb8680 (2020). doi: 10.1126/sciadv.abb8680 [PubMed: 33277246]
62. Mitew S et al. , Focal demyelination in Alzheimer's disease and transgenic mouse models. Acta Neuropathol. 119, 567–577 (2010). doi: 10.1007/s00401-010-0657-2 [PubMed: 20198482]
63. Spires-Jones TL, Hyman BT, The intersection of amyloid beta and tau at synapses in Alzheimer's disease. Neuron 82, 756–771 (2014). doi: 10.1016/j.neuron.2014.05.004 [PubMed: 24853936]

64. Masliah E, Terry RD, Mallory M, Alford M, Hansen LA, Diffuse plaques do not accentuate synapse loss in Alzheimer's disease. Am. J. Pathol. 137, 1293–1297 (1990). [PubMed: 2124413]
65. Hamos JE, DeGennaro LJ, Drachman DA, Synaptic loss in Alzheimer's disease and other dementias. Neurology 39, 355–361 (1989). doi: 10.1212/WNL.39.3.355 [PubMed: 2927643]
66. Saalfeld S, Fetter R, Cardona A, Tomancak P, Elastic volume reconstruction from series of ultra-thin microscopy sections. Nat. Methods 9, 717–720 (2012). doi: 10.1038/nmeth.2072 [PubMed: 22688414]
67. Cardona A et al. , TrakEM2 software for neural circuit reconstruction. PLOS ONE 7, e38011 (2012). doi: 10.1371/journal.pone.0038011 [PubMed: 22723842]
68. Micheva KD, Smith SJ, Array tomography: A new tool for imaging the molecular architecture and ultrastructure of neural circuits. Neuron 55, 25–36 (2007). doi: 10.1016/j.neuron.2007.06.014 [PubMed: 17610815]
69. Saalfeld S, Cardona A, Hartenstein V, Tomančák P, As-rigid-as-possible mosaicking and serial section registration of large ssTEM datasets. Bioinformatics 26, i57–i63 (2010). doi: 10.1093/bioinformatics/btq219 [PubMed: 20529937]
70. Xu F et al. , High-throughput mapping of a whole rhesus monkey brain at micrometer resolution. Nat. Biotechnol. 39, 1521–1528 (2021). doi: 10.1038/s41587-021-00986-5 [PubMed: 34312500]
71. Albelda SM, Muller WA, Buck CA, Newman PJ, Molecular and cellular properties of PECAM-1 (endoCAM/CD31): A novel vascular cell-cell adhesion molecule. J. Cell Biol. 114, 1059–1068 (1991). doi: 10.1083/jcb.114.5.1059 [PubMed: 1874786]
72. Robertson RT et al. , Use of labeled tomato lectin for imaging vasculature structures. Histochem. Cell Biol. 143, 225–234 (2015). doi: 10.1007/s00418-014-1301-3 [PubMed: 25534591]
73. Sawhney R, Crane K, Boundary first flattening. ACM Trans. Graph. 37, 5 (2017). doi: 10.1145/3132705
74. Lee TC, Kashyap RL, Chu CN, Building skeleton models via 3-D medial surface axis thinning algorithms. CVGIP Graph. Models Image Process. 56, 462–478 (1994). doi: 10.1006/cgip.1994.1042
75. Quan T et al. , NeuroGPS-Tree: Automatic reconstruction of large-scale neuronal populations with dense neurites. Nat. Methods 13, 51–54 (2016). doi: 10.1038/nmeth.3662 [PubMed: 26595210]
76. Winnubst J et al. , Reconstruction of 1,000 projection neurons reveals new cell types and organization of long-range connectivity in the mouse brain. Cell 179, 268–281.e13 (2019). doi: 10.1016/j.cell.2019.07.042 [PubMed: 31495573]
77. Banerjee S et al. , Semantic segmentation of microscopic neuroanatomical data by combining topological priors with encoder-decoder deep networks. Nat. Mach. Intell. 2, 585–594 (2020). doi: 10.1038/s42256-020-0227-9 [PubMed: 34604701]
78. Ronneberger O, Fischer P, Brox T, U-Net: Convolutional networks for biomedical image segmentation. arXiv:1505.04597 [cs.CV] (2015). doi: 10.1007/978-3-319-24574-4_28
79. Shit S et al., "clDice–a Novel Topology-Preserving Loss Function for Tubular Structure Segmentation," Proceedings of the IEEE Computer Society Conference on Computer Vision and Pattern Recognition, pp. 16555–16564 (2021). doi: 10.1109/CVPR46437.2021.01629
80. Pollack D et al. , Axon tracing and centerline detection using topologically-aware 3D U-Nets. Annu. Int. Conf. IEEE Eng. Med. Biol. Soc. 2022, 238–242 (2022). doi: 10.1109/EMBC48229.2022.9870879 [PubMed: 36085649]
81. Kanai R, Rees G, The structural basis of inter-individual differences in human behaviour and cognition. Nat. Rev. Neurosci. 12, 231–242 (2011). doi: 10.1038/nrn3000 [PubMed: 21407245]
82. Gao L et al. , Single-neuron projectome of mouse prefrontal cortex. Nat. Neurosci. 25, 515–529 (2022). doi: 10.1038/s41593-022-01041-5 [PubMed: 35361973]
83. Ding SL et al. , Comprehensive cellular-resolution atlas of the adult human brain. J. Comp. Neurol. 524, 3127–3481 (2016). doi: 10.1002/cne.24080 [PubMed: 27418273]
84. Kamentsky L et al., Light sheet imaging of the human brain (Version draft) [Data set], DANDI Archive (2023); 10.80507/dandi.123456/0.123456.1234.

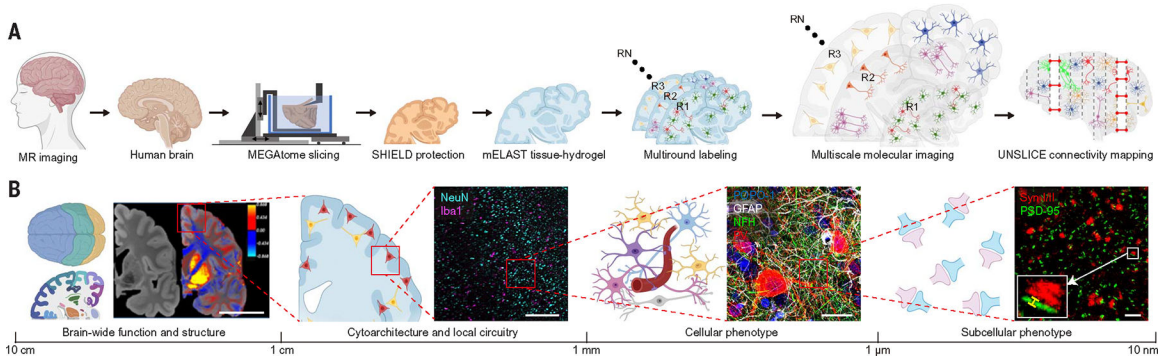

Fig. 1. Integrated platform for multiscale molecular interrogation of the human brain.

(**A**) The workflow of the platform includes slicing, processing, labeling, imaging, and computational stitching of the human brain tissues. After magnetic resonance (MR) imaging, human brain hemispheres are sliced into millimeter-thick slabs using MEGAtome. The slabs are SHIELD-processed and transformed into mELAST tissue-hydrogels. The tough, elastic, and size-adjustable mELAST tissue-hydrogels undergo multiround labeling and imaging at multiple scales to extract high-dimensional features. The images acquired from the sliced human brain tissues are computationally reintegrated using the UNSLICE pipeline for multilevel connectivity mapping. (**B**) 3D multiscale profiling of the human brain captures brain-wide structures, cytoarchitecture and local circuitry, and cellular and subcellular features from the same tissue. Scale bars (from left to right): 5 cm, 300 μm, 25 μm, and 500 nm (inset: 25 nm).

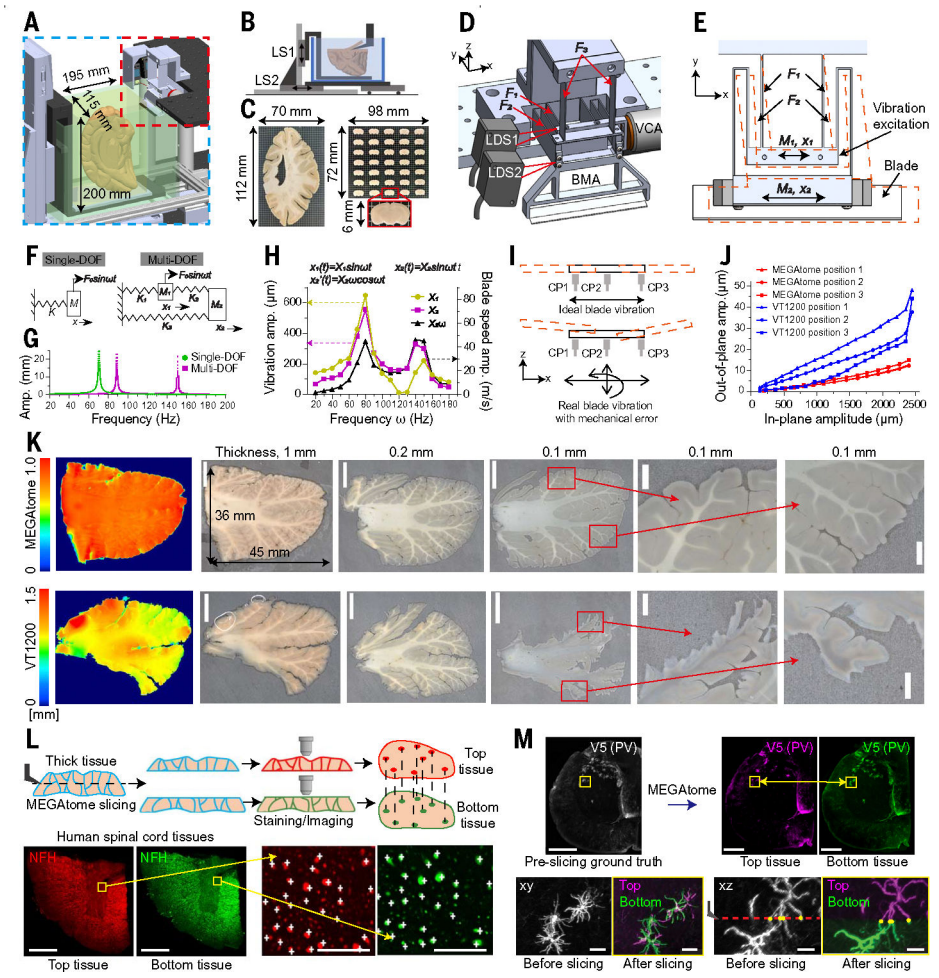

Fig. 2. Mechanical design and characterization of MEGAtome for scalable, information-lossless slicing.

(**A**) MEGAtome consists of two main modules: a blade vibration generation and control platform (in red frame) and a sample mounting and feeding platform (in blue frame). (**B**) The sample mounting and feeding platform is configured through two linear stages (LS1 and LS2). (**C**) MEGAtome-sliced whole human brain hemispheres and mouse brain arrays. (**D** and **E**) Mechanical design of the blade vibration generation and control mechanism shown in a 3D view (D) and in an *xy* plane (E). LDS, laser distance sensor; BMA, blade mounting assembly; VCA, voice coil actuator. (**F**) A single-DOF model (left, typical commercial vibratomes) and a multi-DOF model (right, MEGAtome), in which K_1, K_2, and K_3 represent the stiffnesses of F_1, F_2, and F_3, respectively. (**G**) Simulation results showing the forced vibration response of single- and multi-DOF systems. (**H**) Measurements of vibration amplitude and blade speed of x_1 and x_2 as functions of frequency (hertz). (**I**) Demonstration of ideal and real blade vibration accompanied by parasitic errors. (**J**) Measurements of blade out-of-plane parasitic vibration amplitude versus in-plane vibration amplitude of VT1200 vibratome and MEGAtome. (**K**) MEGAtome and VT1200 generated 1.0-, 0.2-, and 0.1-mm-thick slices from whole human cerebellums. The 1-mm-thick slices were scanned by an optical profiler showing the surface height variance. Scale bars: 10

mm (whole slice figures) and 2 mm (enlarged figures). (**L**) Images of NFH+ axons in the cut surfaces of human brain spinal cord tissues after MEGAtome slicing. Scale bars, 1 mm (left figures) and 40 μm (right enlarged figures). (**M**) Images of V5+ neurons in the PV-Cre MORF mouse brain tissues before and after MEGAtome slicing. Scale bars: 500 μm (top row) and 50 μm (bottom row). The images were obtained with the 20×/0.5 numerical aperture (NA) (L) and 4×/0.2NA objectives (M).

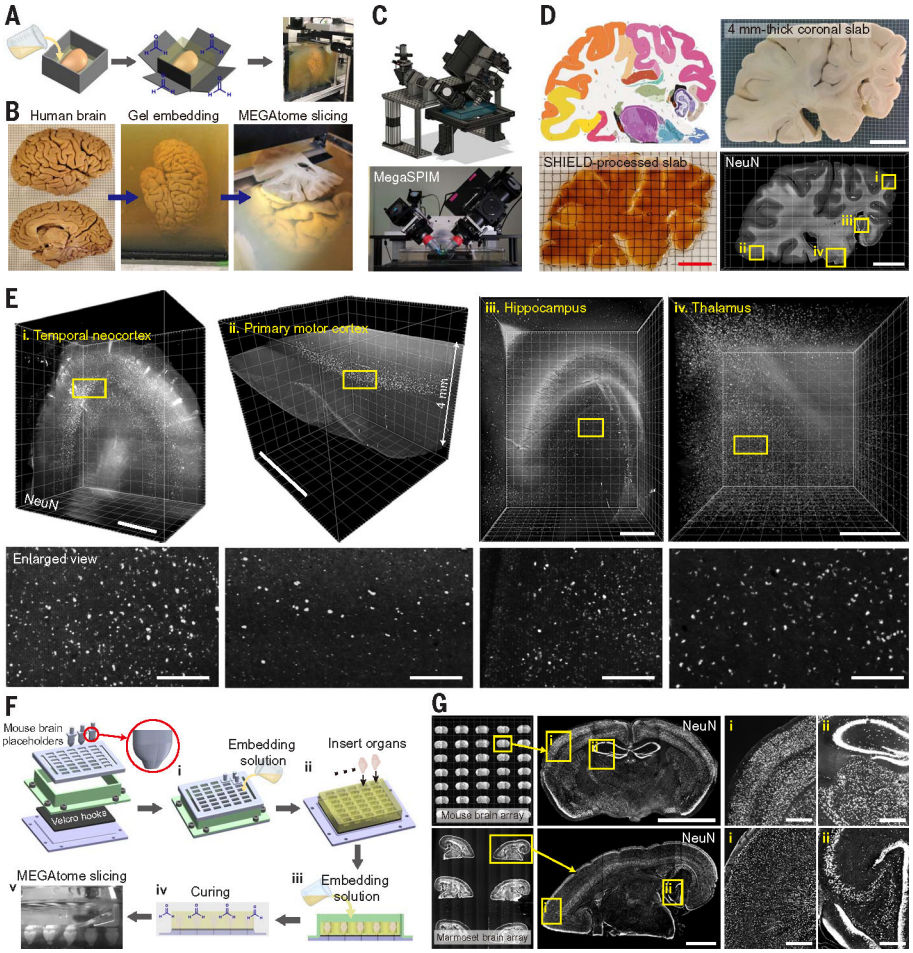

Fig. 3. Large-scale slicing and high-throughput imaging of the whole human brain hemisphere and an array of animal organ–scale tissues.

(**A**) A schematic drawing of the whole mounting of an intact human brain hemisphere for MEGAtome slicing. To gel-embed a whole human brain hemisphere, liquid gel is first poured onto the hemisphere and then solidified, followed by chemical cross-linking of the gel with the brain in PFA (paraformaldehyde) solution. After sufficient cross-linking, the gel with the hemisphere [approximately 65 mm (width) by 180 mm (height) by 130 mm (length)] is mounted onto MEGAtome for slicing. (**B**) A banked human brain hemisphere was embedded in gel and subsequently sliced by MEGAtome. (**C**) MegaSPIM, a rapid, obliquely operated, multicolor light-sheet microscopy for imaging large-scale tissues. (**D**) A 4-mm-thick coronal human brain slab, encompassing multiple cortex regions, hippocampus, striatum, and thalamus, was SHIELD-cleared, immunostained with anti-NeuN antibodies, and imaged intact. Scale bar: 2 cm. (**E**) 3D image volume and enlarged *xy* plan views of NeuN+ cells from each brain region. Scale bars: 3 mm (top row) and 200 μm (bottom row). (**F**) A protocol for gel-embedding of animal organ arrays and their subsequent slicing: (i) Liquid gel is poured over the assembled tools, (ii) animal organs are positioned in the holder, (iii) the organs are completely immersed in extra liquid gel, (iv) the gel-organ mixture is solidified and fixed in PFA, and (v) MEGAtome slices the array. (**G**) Images of NeuN+ neurons from the arrays of 35 mouse brains and six marmoset hemispheres. Scale bars:

3 mm (second column) and 500 mm (enlarged view). The images were obtained with the 2×/0.1NA objective [(D), (E), and (G)]. Anatomical annotations in (D) are from Allen Brain Reference Atlases (Adult Human, Modified Brodmann; http://atlas.brain-map.org) (83).

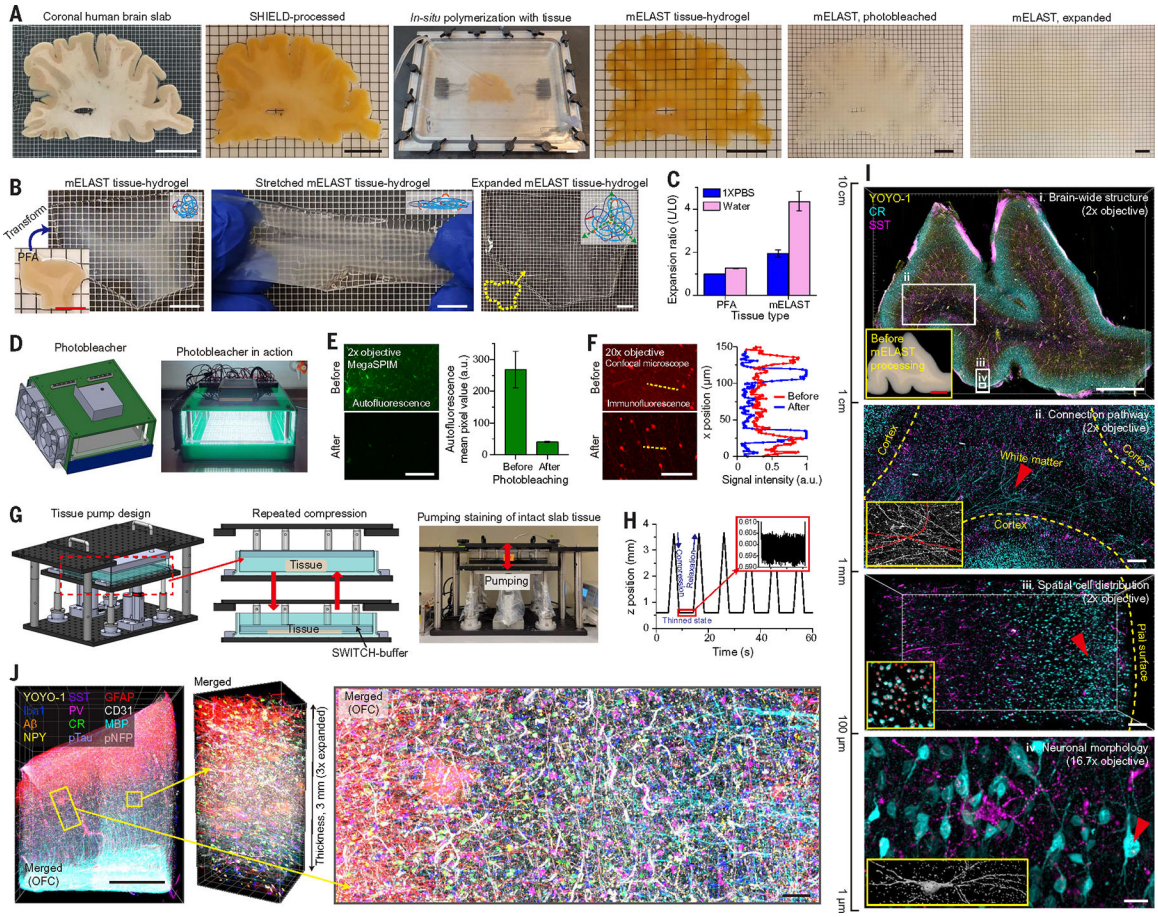

Fig. 4. mELAST tissue-hydrogel processing platform for multiplexed multiscale molecular imaging of the human brain.

(**A**) The workflow of mELAST tissue-hydrogel processing for an intact coronal human brain slab. Scale bar: 2 cm. (**B**) The elastic and expandable mELAST human brain tissue-hydrogel. Scale bar: 1 cm. (**C**) Expansion ratios of PFA tissues and mELAST tissue-hydrogels in 1XPBS (phosphate-buffered saline) and water. L_0 is the mean length of the original brain, and L is the mean length in 1XPBS or water. Error bars show mean ± SD (n = 5). (**D**) A photobleaching device to remove autofluorescence from lipofuscin and other autofluorescence pigments in human brain tissues. (**E**) Images and mean pixel values of the background autofluorescence signal from human brain tissues captured by MegaSPIM before and after photobleaching. Scale bar: 300 μm. a.u., arbitrary units. Error bars show mean ± SD (n = 6). (**F**) Images of immunolabeled CR+ neurons from the photobleached and nonphotobleached human brain tissues. The graph shows the signal intensity measured from the yellow dashed lines in each image. Scale bar: 100 μm. (**G**) A human brain–scale tissue pump for accelerated clearing, washing, staining, and destaining of large-scale mELAST tissue-hydrogels. (**H**) A graph measures the distance between the pump head and the chamber floor during the operation of the pump. The inset graph shows the enlarged view. (**I**) Multiscale imaging of an mELAST-processed and SWITCH-pumping-stained intact coronal human brain hemisphere tissue (size in 5.8 cm by 4.2 cm by 2.5 mm). Each red arrowhead indicates the magnified area within the insets. Scale bars (top to bottom): 5 mm,

1 mm, 200 μm, and 20 μm. (**J**) Highly multiplexed imaging of an mELAST human brain tissue, simultaneously mapping neuronal and non-neuronal cell subtypes. Scale bars: 2 mm (left figure) and 100 μm (enlarged view). The images were obtained with the 2×/0.1NA [(E), (I) i, ii, iii, and (J)], 20×/0.5NA (F), and 16.7×/0.4NA objectives [(I), iv].

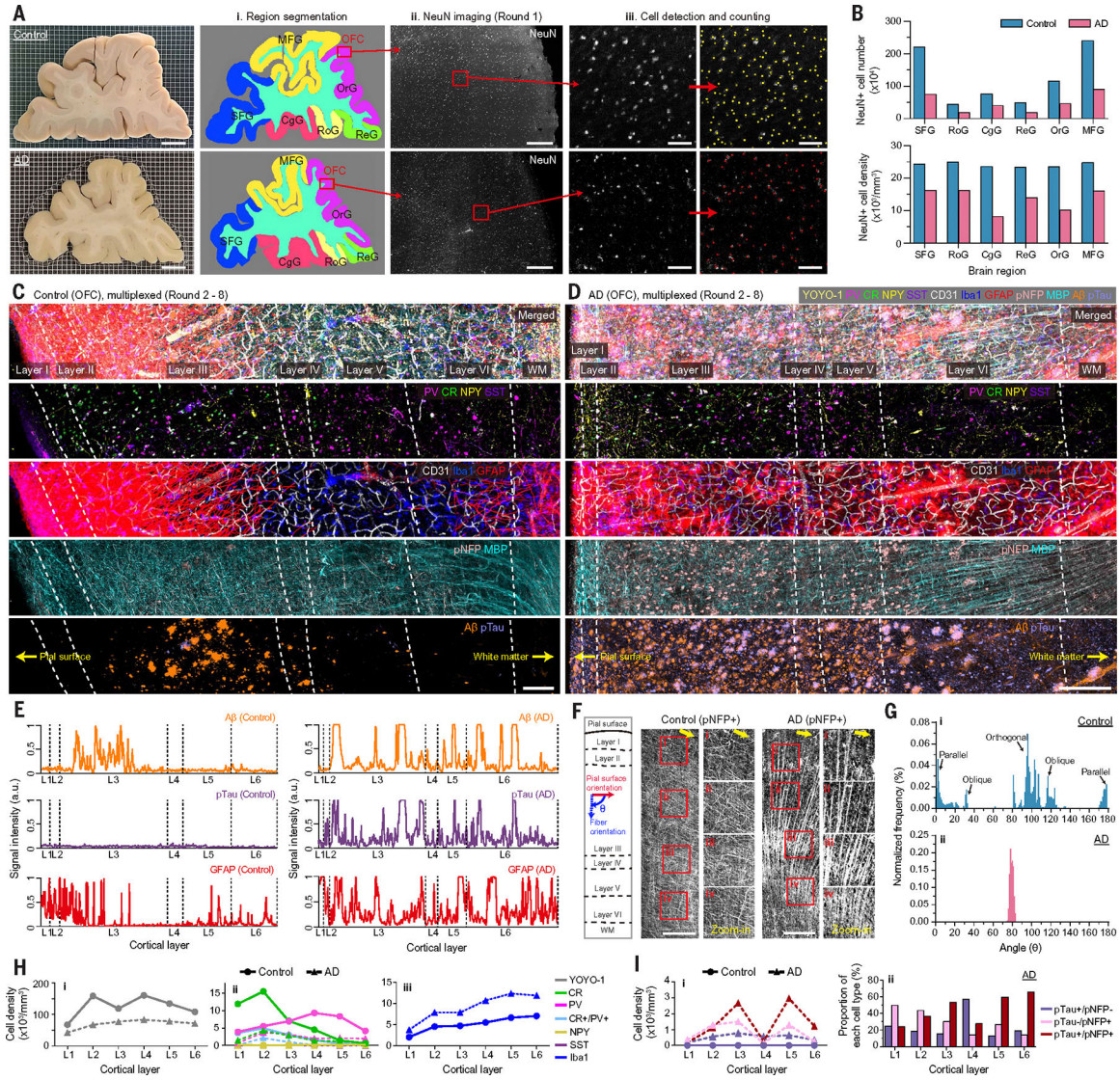

Fig. 5. Comparative single-cell resolution imaging and phenotyping of the human brains.

(**A** and **B**) Holistic quantitative analysis of individual cells in large tissue volumes. (A) Images of immunolabeled NeuN+ cells in the slabs that include cerebral gyri [superior frontal gyrus (SFG), rostral gyrus (RoG), cingulate gyrus (CgG), gyrus rectus (ReG), orbital gyrus (OrG), and mid frontal gyrus (MFG)], from both control and AD cases. (i) Segmented cortical subregions in the whole slab images, (ii) enlarged views of orbitofrontal cortex (OFC) from OrG, and (iii) NeuN+ cells detected and automatically counted for each cortex subregion. Scale bars: 1 cm (first column), 500 μm (third column), and 100 μm (fourth and fifth columns). (B) The graphs show number and density of NeuN+ cells across each brain subregion of the two cases. (**C** and **D**) Multiplexed staining and imaging of mELAST-processed human brain tissues from the OFC in control and AD slabs, described in (A): nuclei (YOYO-1), neuronal subtypes (PV, CR, NPY, and SST), astrocytes (GFAP), microglia (Iba1), oligodendrocytes (MBP), axons (pNFP), endothelial cells (CD31), senile plaques (Aβ), and neurofibril tangles (pTau). Scale bar: 200 μm. (**E**) Comparative signal intensity

profiles of GFAP, Aβ, and pTau across the cortical column from the two cases. (**F** and **G**) pNFP+ cortical fiber orientation analysis. WM: White matter. (F) Representative images of pNFP+ fibers throughout the cortex of the control and AD tissues (yellow arrows represent the pial surface direction). Scale bar: 300 μm. (G) Histograms of the angular orientation of pNFP+ fibers with respect to the cortical column direction (θ) in the control and AD tissues. (**H**) Layer-specific comparison of the density and distribution of (i) YOYO-1; (ii) PV+, CR+, NPY+, SST+, CR+/PV+ neurons; and (iii) Iba1+ microglia in the OFC of the control and AD tissues. (**I**) Analysis of the spatial distribution pattern of cells associated with pTau and pNFP. Layer-specific comparison of (i) cell density and (ii) proportion of each subtype of pTau+/pNFP−, pTau−/pNFP+, and pTau+/pNFP+ cells in each layer. The images were obtained with the 2×/0.1NA objective [(A), (C), (D), and (F)].

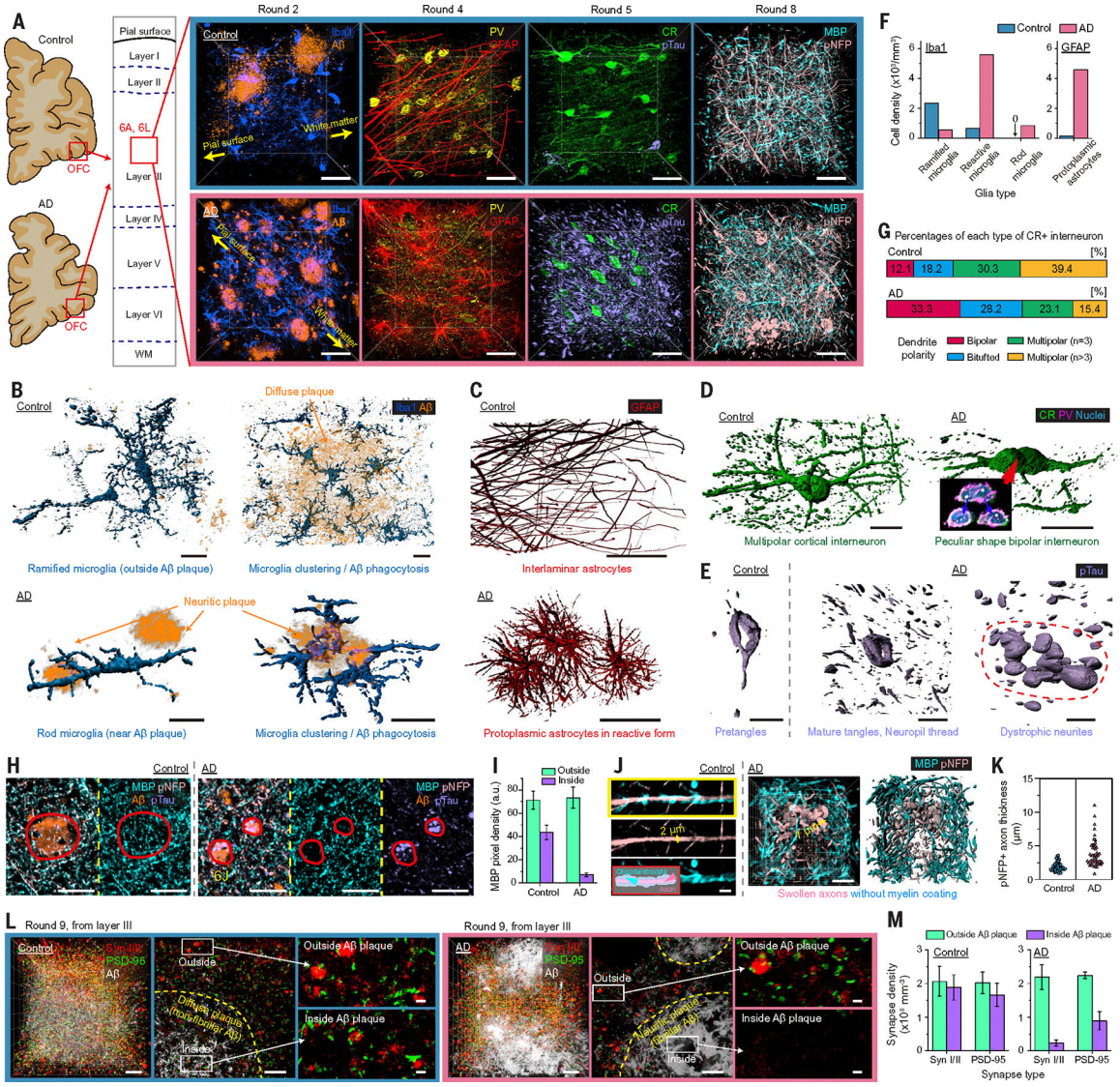

Fig. 6. Comparative subcellular resolution imaging and phenotyping of the human brains.

(**A**) Fine morphological details of cells in the same expanded mELAST tissue-hydrogels (layer III) described in Fig. 5, C and D. Scale bar: 50 μm. (**B** to **E**) Comparison of the detailed morphology of each cell type, illustrated with representative 3D rendering images: (B) Iba1+ microglia and associated Aβ plaques (scale bar, 20 μm), (C) GFAP+ astrocytes (scale bar, 50 μm), (D) CR+ and CR+/PV+ neurons (scale bar, 20 μm), and (E) pTau+ cells and fibers (scale bar, 20 μm). (**F**) Cell density of each glia type classified on the basis of its morphology. (**G**) Percentages of CR+ interneurons in the control and AD cases, classified by their dendrite morphology: bipolar, bitufted, multipolar ($n = 3$), and multipolar ($n > 3$). (**H** to **J**) Multiscale imaging and analysis of axonal damage. (H) Representative single-cell resolution images of pNFP+ axons, MBP+ oligodendrocytes, pTau+ fibers, and Aβ plaques. Scale bar: 50 μm. (I) Analysis of MBP pixel density from regions inside and outside Aβ plaques in the control and AD tissues. Error bars show mean ± SD ($n = 10$). (J) pNFP+ axon and MBP+ oligodendrocyte morphology at the subcellular level, represented by the marked

region in (H). Scale bars: 5 μm (left figure) and 20 mm (right figure). (**K**) Distribution of thickness of representative pNFP+ axons in the control and AD tissues ($n = 50$). (**L**) 3D mapping of nanoscopic chemical synapses (Syn I/II and PSD-95) and Aβ+ plaques in the same 4.5× expanded control and AD mELAST-processed human brain tissue-hydrogels described in (A). Scale bars: 5 μm and 500 nm (zoom-in view). (**M**) Comparison of the density of Syn I/II and PSD-95 in the control and AD tissues, both inside and outside Aβ plaques. Error bars show mean ± SD ($n = 10$). The images were obtained with the 2×/0.1NA (H), 16.7×/0.4NA [(A) to (E), and (J)], and 63×/1.2NA objectives (L).

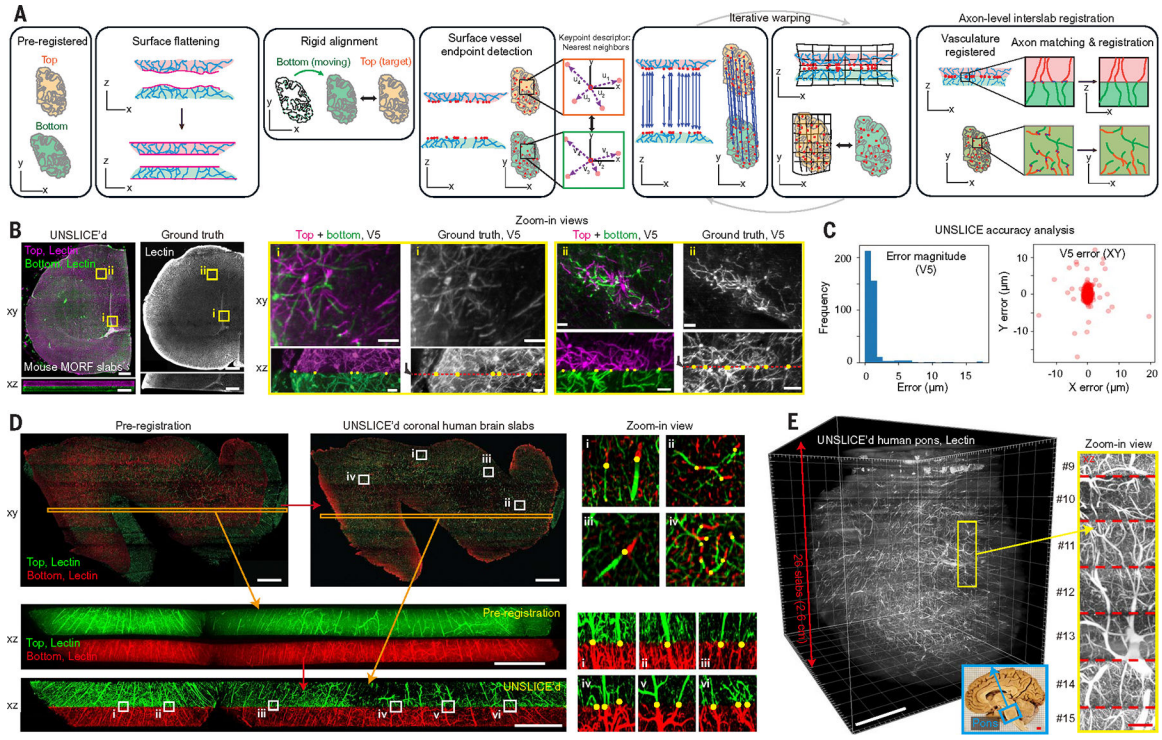

Fig. 7. UNSLICE computational pipeline for accurate multilevel interslab registration of the large-scale sliced tissue blocks.

(**A**) Schematic of the UNSLICE pipeline. (**B**) 3D reconstruction of genetically labeled PV+ neurons in MORF mouse brains using UNSLICE. Scale bars: 500 µm (macroscopic view) and 50 µm (zoom-in views). (**C**) Quantification of the distance (error) between fiber endpoints at the cut surface in three sampled subsections, based on ground-truth image data before and after slicing at cellular resolution (average error: ~1.29 µm). (**D**) UNSLICE registration of two adjacent coronal human brain hemisphere slabs, based on vascular endpoints (lectin channel) of the consecutive slabs (*xy* and *xz* optical cross sections). Scale bar: 2 mm. Inset images show blood vessels connected across the cut surface. Scale bar: 2 mm. (**E**) 3D rendering of a fully reconstructed human pons. Scale bar: 1 cm. A zoomed-in view of the *xz* plane to show the registered vasculature at multiple interfaces. Scale bar: 500 µm. The images were obtained with the 2×/0.1NA [(D) and (E)] and 4×/0.2NA (B) objectives.

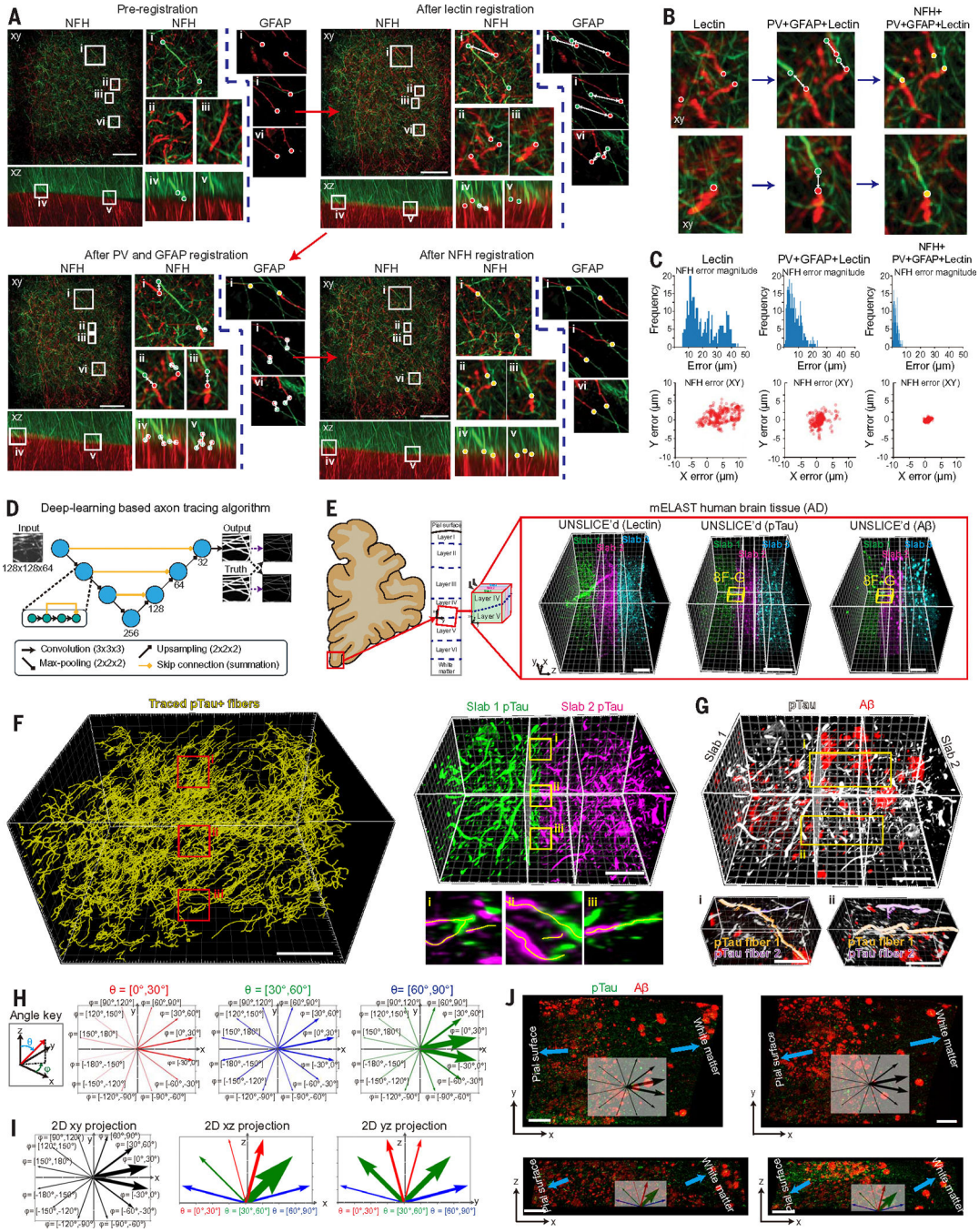

Fig. 8. Multichannel interslab registration and volumetric axon tracing for single-fiber–level connectivity mapping in the human brain.

(**A**) Multichannel interslab registration at single-fiber resolution using NFH+ and GFAP+ fibers within a single field of view of the larger cortical tissue. Scale bar: 100 μm. Inset images depict maximum intensity projections (MIP) of NFH+ and GFAP+ fibers in *xz* and *xy* planes. (**B**) NFH+ fibers from the same field of view to show progression of co-registration during each registration step, including vasculature (lectin) registration, PV/GFAP fine-tuning, and NFH fine-tuning. (**C**) Histogram of absolute errors (top) and *x*-*y*

lateral connectivity errors (bottom) for NFH+ fibers during each registration step. (**D** to **J**) pTau+ fiber mapping and phenotyping in AD human brain tissue. (D) A deep-learning based axon tracing algorithm for end-to-end detection of axon centerlines using a residual 3D U-Net architecture. (E) An mELAST-processed AD human brain tissue was reconstructed with UNSLICE at single-fiber level. Scale bar: 0.5 mm. (F) Automated volumetric tracing of pTau+ fibers across cut human brain tissue slices. The right figure and zoomed insets i to iii show MIP overlaid with tracing results. Scale bar: 150 μm. (G) An Aβ (red)/pTau (grayscale) overlay of the same subvolume from (F). Insets i and ii: zoomed-in subvolumes depicting two segmented long traced pTau+ fibers among Aβ plaques. Scale bar: 150 μm. (H) pTau+ fiber orientation histogram of the traced fibers from the subvolume in (F), binned by polar (φ) and azimuthal angle (θ). The thickness of each vector was proportional to fiber counts in each direction. (I) Histograms from (H) projected into the 2D *xy*, *xz*, and *yz* planes. (J) The *xy* and *xz* plane views to show the fiber orientation to the cortical column. The images were obtained with the 20×/0.5NA [(A) and (B)] and 16.7×/0.4NA [(E) to (G), and (J)] objectives.